Journal Pre-proof

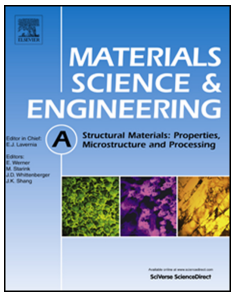

Optimisation of process parameters for an additively manufactured AlSi10Mg alloy: limitations of the energy density-based approach on porosity and mechanical properties estimation

Maverick Giovagnoli, Giacomo Silvi, Mattia Merlin, Maria Teresa Di Giovanni

PII: S0921-5093(20)31676-2

DOI: https://doi.org/10.1016/j.msea.2020.140613

Reference: MSA 140613

To appear in: *Materials Science & Engineering A*

Received Date: 12 May 2020

Revised Date: 5 November 2020

Accepted Date: 29 November 2020

Please cite this article as: M. Giovagnoli, G. Silvi, M. Merlin, M.T. Di Giovanni, Optimisation of process parameters for an additively manufactured AlSi10Mg alloy: limitations of the energy density-based approach on porosity and mechanical properties estimation, *Materials Science & Engineering A*, https://doi.org/10.1016/j.msea.2020.140613.

This is a PDF file of an article that has undergone enhancements after acceptance, such as the addition of a cover page and metadata, and formatting for readability, but it is not yet the definitive version of record. This version will undergo additional copyediting, typesetting and review before it is published in its final form, but we are providing this version to give early visibility of the article. Please note that, during the production process, errors may be discovered which could affect the content, and all legal disclaimers that apply to the journal pertain.

© 2020 Elsevier B.V. All rights reserved.

Journal Pre-proof

Optimisation of process parameters for an additively manufactured AlSi10Mg alloy: limitations of the energy density-based approach on porosity and mechanical properties estimation

Maverick Giovagnoli[a]*, Giacomo Silvi[a], Mattia Merlin[a], Maria Teresa Di Giovanni[b]

[a] University of Ferrara, Department of Engineering, via Saragat 1, 44122 Ferrara, Italy

[b] AMT S.r.l, via Morello di Mezzo 100/140, Camposanto, Italy

* Corresponding author: Maverick Giovagnoli, maverick.giovagnoli@unife.it

Abstract

Due to the high complexity of the Additive Manufacturing processes, the effect of individual deposition parameters on integrity and mechanical performance of the 3D-printed part is not easily assessable. An energy density-based approach is often adopted to overcome such complexity, being the Volumetric Energy Density (VED) one of the widely used parameters. However, previous works on the AlSi10Mg alloy suggest that fully dense parts could be achieved with a well defined VED range. This study investigates different combinations of deposition parameters to reproduce part of this range and assess its effect on porosity, microstructure and tensile properties of the AlSi10Mg alloy. It was found that different combinations of deposition parameters in the employed VED range did not alter the microstructural features significantly. Conversely, they severely affected porosity, showing that VED is not a reliable parameter to predict the final density of the additively manufactured components. Moreover, specimens produced with a similar VED but different hatch spacing exhibit significantly different tensile properties. This fact suggests that the effect of deposition parameters should not be solely related

to the amount of energy imparted to the material. Finally, systematically higher tensile properties characterise our specimens compared to results available in the literature, due to the microstructure obtained with the adopted combination of deposition parameters. The energy density-based approach lacks in considering the effect of process parameters on the microstructural features other than porosity, which could identify their actual proper combination misleadingly. Our results suggest that new approaches to define the optimum choice of process parameters need to be evaluated to maximise the final performance of AM components.

Keywords: Additive manufacturing, AlSi10Mg, process parameters, VED, microstructure, mechanical characterisation

1. Introduction

Among the manufacturing processes, Additive Manufacturing (AM) represents one of the most attracting technologies of the last decade in both academic and industrial fields. The unlimited flexibility in the design of complex-shaped components, the increasing need for optimised use of raw materials and minimisation of machining operations and scraps, have led to an increasing interest in such a topic. Currently, among the AM process, the Direct Metal Laser Solidification (DMLS) laser powder bed fusion technology is one of the most successfully employed for metal components production.

The Al alloys represent one of the most widely employed metallic materials in the AM processes. They are particularly suitable for structural components which require a reasonable compromise between mechanical performances and light-weighting as well as for heat-controllable parts which need for high thermal conductivity, such as heat exchangers and heat sinks. In light of this, Al alloys are considered very promising for aerospace and automotive

applications. Among all, the AlSi alloys offer the best processability, especially at Si contents near to the eutectic composition. In recent years, the AlSi10Mg alloy has been extensively investigated [1,2]. Thijs *et al*. [3] correlated the fine cellular microstructure with a preferred crystallographic texture with the high mechanical response. Wu *et al*. [4] performed in-situ TEM compression tests to elucidate the reasons for such strength. Maeshima *et al*. [5] proved the existence of a large amount of Si retained in solid solution in the Al phase as additional contributions to the strength of the alloy. Liu *et al*. [6] highlighted that the texture of the alloy could be modified through the building parameters. Despite the broadening of Al alloys palette for the AM technologies is a recent research topic [7–9], the AlSi10Mg alloy is still one of the most employed.

Although the strength of the Al alloys produced with the AM techniques, their mechanical performances can be severely affected by the presence of process-related defects, with porosity being the most deleterious one [10–12]. It descends from a non-optimised process, and hence a proper choice of the building parameters is mandatory to achieve a near fully dense final component. Even though the high number of parameters that take part at the overall AM process, just a few of them are commonly investigated, namely: the laser power, the scan speed of the energy source, the hatch spacing and the layer thickness. An energy density-based approach is usually adopted in the literature to account for such process parameters, with the minimum porosity achieved within a specific window of energy density. Inside the optimum window, an almost entirely dense part is obtained, whereas too low or too high energy density leads to lack-of-fusion and keyhole porosities, respectively [13–15]. Kempen *et al*. [16] optimised the deposition of an AlSi10Mg alloy based on an energy per unit length parameter E' [J/mm], defined as the ratio of laser power and scan speed. A superficial energy density E_d [J/mm^2] was employed by Krishnan *et al*. [17] to minimise the porosity for the same alloy. However, a volumetric energy density (VED)

parameter is often used to define a proper process window [11,18–20], with the VED [J/mm^3] defined as equation (1):

$$VED = \frac{P}{v \cdot h \cdot t} \quad (1)$$

where P [W] is the laser power, v [mm/s] is the scan speed, h [mm] is the hatch spacing, and t [mm] is the layer thickness. Read *et al*. [20] found that ~60 J/mm^3 of VED was suitable to achieve a dense AlSi10Mg alloy. A similar optimum value was determined by Kimura *et al*. [19] processing an AlSi7Mg alloy. Despite such agreement, data in the literature are somewhat scattered. Figure 1 depicts the optimum density obtained for several Al-Si alloys (Si ≥ 7%) and the correspondent VED range or value [2,10,12,16–25]. For works not directly referring to the energy density, the VED was calculated using the optimised building parameters accordingly to equation (1). VEDs in the range 30-110 J/mm^3 were found to be suitable to achieve fully dense parts (relative density in the range 98-99.9%), with the majority of the data lying between 40 and 70 J/mm^3. It is worth to notice that the works reported in Fig. 1 majorly deal with the effect of the energy density on porosity of the alloys, with little or no attention to the other microstructural features and their effect on the resulting mechanical properties.

The present work starts from an actual industrial need to determine the proper combination of process parameters for the AlSi10Mg alloy in light of the final tensile performance and based on data available in the literature. It aims at verifying the reliability of the energy density-based approach commonly adopted in the literature, with particular reference to the VED, in defining the optimum process window of deposition parameters. Additionally, it seeks to assess the reproducibility of tensile properties for specimens produced within a given energy density range. Therefore, we investigated the effect of VED in the above-mentioned range (40-70 J/mm^3) on porosity, microstructure and mechanical performance of the AlSi10Mg alloy and to validate its

effectiveness as a proper design parameter. Our results highlight some severe limitations of such an approach and elucidate the need for further research in this field.

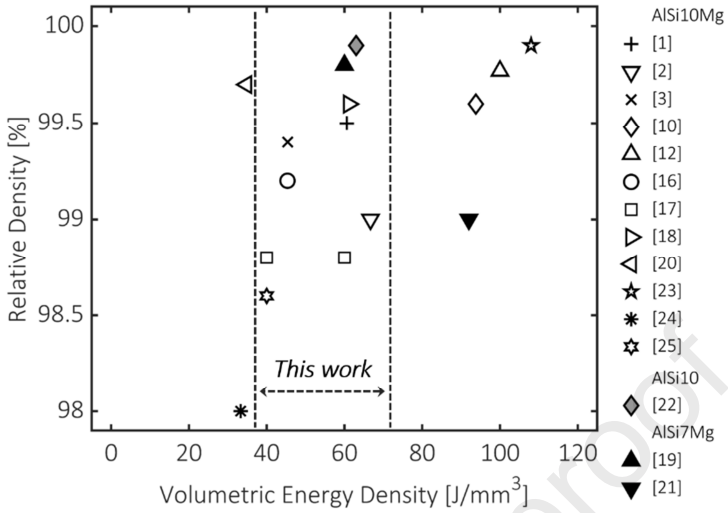

Figure 1. Comparison of literature data for different Al-Si alloys: VED ranges/values that achieved fully dense components (relative density in the range 98-99.9%).

2. Experimental

2.1 Additively manufactured samples

The samples were produced with an EOS M290 system using the Direct Metal Laser Solidification (DMLS) laser powder bed fusion technology. A commercially available AlSi10Mg powder was processed in a protective argon atmosphere on a cold-building platform. All the specimens were realised at constant laser power (P) and layer thickness (t). Different combinations of scan speed (v) and hatch spacing (h) are reported in Table 1, together with the corresponding VED. Absolute values of process parameters cannot be disclosed, as reported in other scientific researches performed in collaboration with industry [26]. Hence, in Tab. 1 they are reported normalised to the corresponding minimum value.

Journal Pre-proof

Journal Pre-proof

Table 1. Combinations of building parameters - scan speed and hatch spacing - and corresponding VED

v [mm/s]	v	1.18 · v	1.36 · v	1.55 · v	v	1.18 · v	1.36 · v	1.55 · v
h [mm]	h	h	h	h	1.12 · h	1.12 · h	1.12 · h	1.12 · h
VED [J/mm^3]	66	56	48	42	59	50	43	38

For each condition, three cylindrical tensile specimens were produced vertically to the building platform and then machined to the final size (diameter d_0 = 4 mm, gage length L_0 = 20 mm). An additional 10 x 10 x 25 mm^3 cuboid sample was realised with the long side parallel to the building platform for each condition. Microstructural and mechanical characterisations were performed on specimens in the as-built state.

2.2 Tensile tests, Brinell hardness and density measurements

Tensile tests were performed using an Instron 5982 testing machine, according to the ISO 6892-1: 2016 standard. Density measurements were conducted on the cuboid samples with the hydrostatic weighing method using a METTLER AE240 analytical scale. Samples were firstly weighed in air and then in distilled water. Absolute density values were obtained as the average of five measurements. Relative densities were calculated from the absolute ones as the ratio with the nominal alloy density, considered as 2.67 g/cm^3 according to [27]. Brinell hardness tests were carried out on the lateral sides of the cuboid samples. The measurements were conducted using an ERNST AT130 DR hardness tester, with a load of 62.5 kg$_f$ and a 2.5 mm diameter spherical indenter, according to the UNI EN ISO 6505-1: 2015 standard.

2.3 Microstructural Characterization

Thin sections were cut from the cuboid samples and subjected to standard metallographic preparations. To further support the density measurements, the porosity of unetched specimens was investigated using image analysis with a Leica DMI 5000M optical microscope (OM). The relative density was calculated as the percentage of the analysed surface not occupied by the porosity. Size and morphology of the pores were evaluated respectively through the Equivalent Diameter (ED) [μm] and Circularity (C) parameters, accordingly to the following expressions:

$$ED = \left(\frac{4 \cdot A}{\pi}\right)^{1/2} \quad (2)$$

$$C = \frac{4 \cdot \pi \cdot A}{P^2} \quad (3)$$

where A [μm^2] is the area of the pores and P [μm] their perimeter. Samples were subsequently etched for 10 s with a 1% HF distilled water solution. Microstructural and fractographic observations were performed with a Zeiss EVO MA 15 scanning electron microscope (SEM) on cuboid and fractured tensile samples, respectively. Size and spacing of microstructural and fractographic features were measured with the software ImageJ. The width of grains and Al cells and the ED of Si particles and pores were assumed as representative size parameters, whereas the spacing of Si particles and dimples was measured with the 3-Nearest Neighbours Distance (3NND) method. X-ray diffraction (XRD) tests were performed on the polished top surface of cuboid samples in a Bragg-Brentano geometry with a Bruker D8 Advance diffractometer equipped with a Cu filament (Kα, 1.5406 Å). Data were acquired in the 2ϑ range from 20 ° to 110 °, with a step-size of 0.02 ° and a step-time of 1 s. Quantitative measurements were computed with the Rietveld refinement method using the software Maud [28]. A 3-parameter harmonic function was used to account for the presence of texture and reduce the error in quantitative measurements.

3. Results and Analyses

3.1 Level of porosity and density

Figures 2a-b-c depict representative OM micrographs of samples produced with low, intermediate and high VED, respectively. At 43 J/mm^3 (Fig. 2a) the sample exhibits a low number of pores, most of which being a few tens of μm in size. As VED increases to 56 J/mm^3, large circular pores, several tens of μm wide, appear. Mostly large pores up to 100-200 μm in size and mainly located at the bottom of melt pools characterises the sample processed with 66 J/mm^3. In addition to keyhole pores, other defects were sometimes detected in the as-built material, like Mg-based oxides and small shrinkage voids. They were found in a small number in all the investigated samples, with a size generally smaller than large keyhole pores. Accordingly, their effect on the final properties was assumed to be negligible and will not be discussed furtherly.

Image analysis was carried out to determine ED and C of pores, and Fig. 2d reports the Probability Density Functions (PDF) of such parameters of samples in Figs. 2a-b-c. At low VED, the ED statistical distribution is narrow and located in the range of a few tens of μm. As VED raises, the distributions gradually flatten and broaden to higher ED values, which mirrors the appearance of larger pores in Figs. 2b-c. Conversely to ED, the C statistical distributions slightly narrow as VED increases. Most of the pores in each sample range between 0.7-0.9 of C, indicating a nearly circular morphology.

Journal Pre-proof

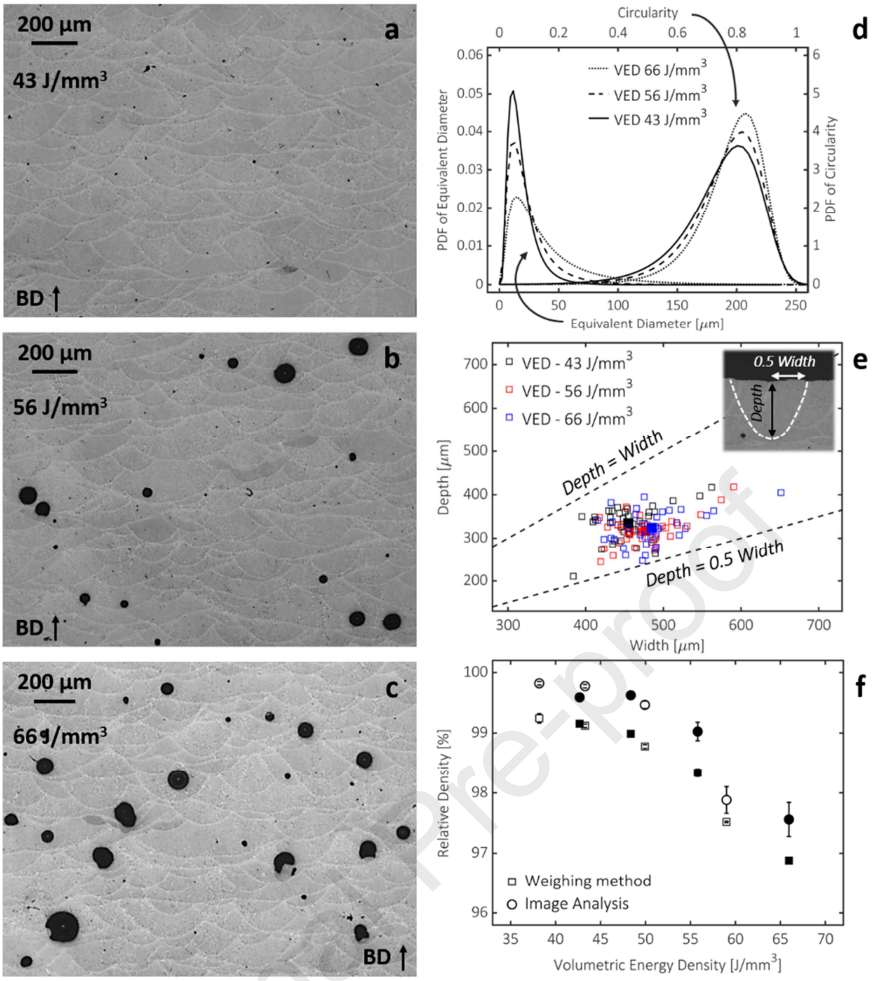

Figure 2. OM micrographs of samples produced with different VED: (a) 43 J/mm³, (b) 56 J/mm³, (c) 66 J/mm³, vertical arrows point out the building direction (BD). (d) ED and C statistical distributions of pores of samples in (a), (b) and (c). (e) Aspect ratio of the melt pools. (f) Relationship between VED and relative density, filled and open markers correspond to hatch spacing h and 1.12 h, respectively. Standard deviation is reported as error bar.

King *et al.* [29] proposed a geometrical criterion to assess the heat transfer mode operating during the deposition of an AISI 316L alloy. A depth-to-width ratio of the melt pool of 0.5 is the threshold between conduction (< 0.5) and keyhole (> 0.5) modes. The same criterion was also adopted for Al alloys [30]. The depth-to-width ratio of melt pools of the top layer was evaluated to avoid multiple overlaps and accurately measure their size. Figure 2e shows that all data of samples

previously mentioned range between 0.5 and 1 of depth-to-width ratio, with no significant effect of VED, suggesting a keyhole heat conduction mode.

Figure 2f reports the relationship between VED and the relative density. Measurements by the weighing method are always ~0.5% lower than by image analysis. A lower size threshold of 70 μm^2 (ED ~10 μm) was applied to pores which suffer from limited resolution during image analysis. Additionally, the corresponding relative density stems from an area measurement, while the weighing method measures the whole sample. These observations could justify the difference mentioned above. However, both methods provide the same trend, with the relative density progressively reducing as VED increases. The highest value of 99.8-99.3% was reached with a VED of 38 J/mm^3, and it falls to 96.5-97.5% as the energy density reached 66 J/mm^3. The distinction between filled and open markers in Fig. 2f is related to the two employed h. It appears that the progressively deteriorating effect of building parameters (v and h) on the relative density can be described with a univocal function of the energy density.

3.2 Microstructural and X-ray diffraction analyses

Although VED in the analysed range considerably affects porosity, its effect on the microstructure was much less evident. Accordingly, Fig. 3 depicts typical features of the sample processed with parameters 1.55v-h, taken as the reference. The AlSi10Mg alloy exhibits a hierarchical microstructure, with the melt pools that occupy the outer level (Fig. 3a). They are delimited by melt pool boundaries, coarse zones produced with a low local cooling rate during the solidification process, highlighted by black arrows in Fig. 3a. Inside the melt pools, the channelling contrast of back-scattered electrons reveals large columnar grains elongated toward the building direction (Fig. 3b). These grains are 5-20 μm wide and up to 200 μm long, and often epitaxially grow across several melt pools. Each grain is made up of a continuous network of fibrous eutectic

Si that surrounds small α-Al cells, marked by black and white arrows in Fig. 3c, respectively. These micrometric cells are about one order of magnitude smaller than grains in Fig. 3b, with which they share the same elongated axis. The amount of eutectic phase, calculated as ~20 ± 4% by image analysis, is far distant from the one expected for an AlSi10 alloy (~75%). Nano-sized Si precipitates, hosted inside the α-Al cells, occupy the inner level of the hierarchical microstructures. They exhibit both globular and acicular morphology, as highlighted respectively by white and black arrows in Fig. 3d, and are tens of nm in size. They could either result from a reduced solubility of Si inside the α-Al cells during the cooling process or precipitation-induced phenomena caused by the neighbouring laser scans. The lack of Mg-containing phases suggests the element to be retained in solid solution inside the α-Al phase.

Journal Pre-proof

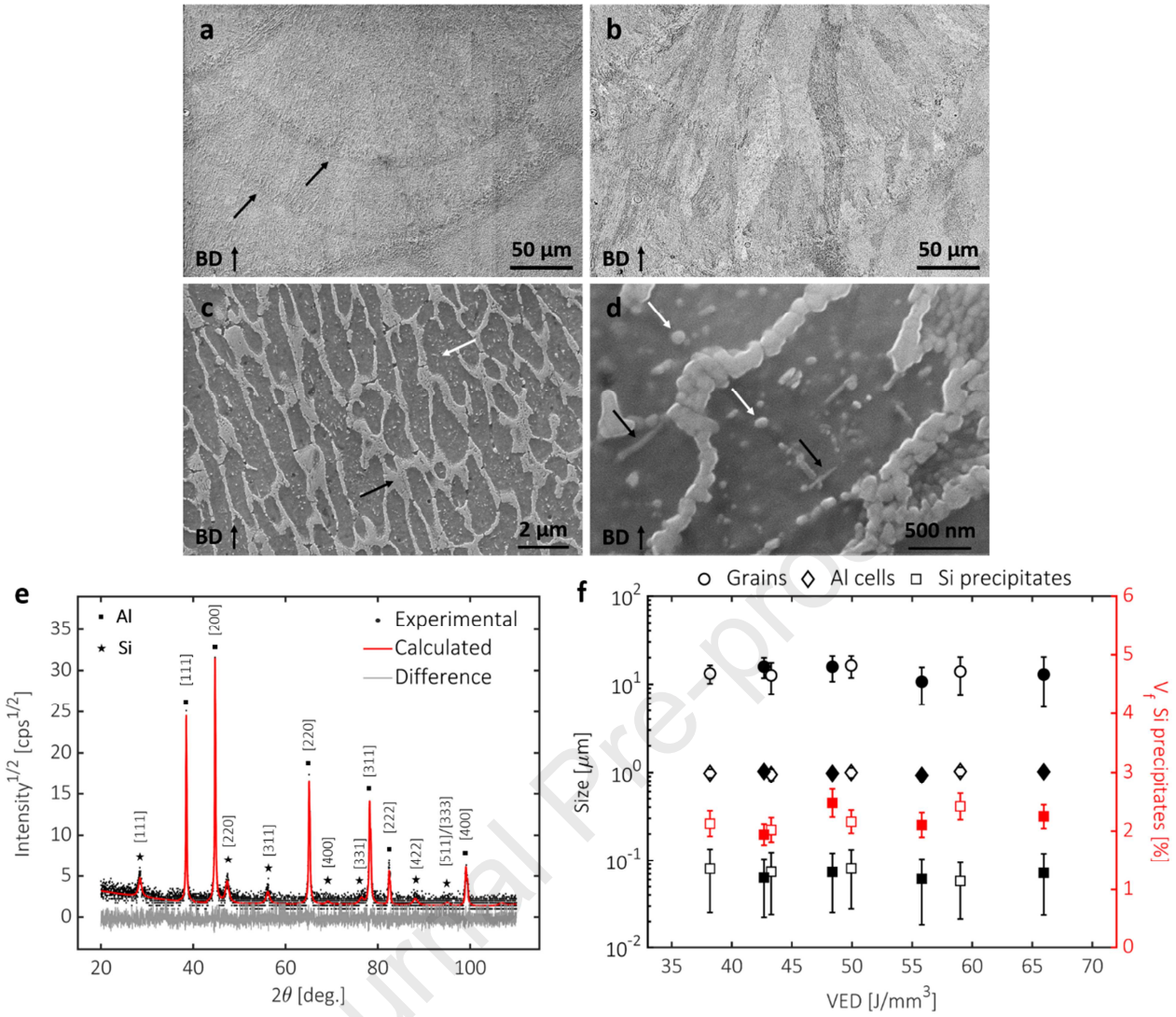

Figure 3. SEM micrographs of the AlSi10Mg alloy, vertical arrows point out the building direction (BD). (a) Melt pool boundaries highlighted by black arrows. (b) Same region as in (a), epitaxial columnar grains. (c) Al cells (white arrow) and eutectic network (black arrow). (d) Nano-sized Si precipitates with globular (white arrow) and acicular (black arrow) morphology. (e) Experimental and calculated XRD patterns. (f) Microstructural features with different VED values. Filled and open markers correspond to hatch spacing h and 1.12h, respectively. Standard deviation is reported as error bar. The reduced standard deviation is not visible in size measurements of Al cells.

1

2 XRD analyses furtherly confirmed the existence of a non-equilibrium microstructure suggested

3 by SEM investigations. As an example, Fig. 3e reports the experimental (dotted) and simulated

(solid) diffraction patterns of the 1.55v-h sample. Following SEM observations, none of the experimental peaks matched with an Mg-bearing constituent. Therefore, the simulated pattern accounts only for the Al and Si phases. The difference curve lies around the zero value and shows that experimental and simulated patterns match well. Instead of the Al [111] being the strongest peak in the diffraction pattern, a pronounced crystallographic texture is present, with the Al [200] reflection being the most intense. Quantitative calculations pointed out some deviations from the equilibrium conditions. A lattice parameter of 4.0498 ± 0.0040 Å was measured for the α-Al phase, which is quite lower than the equilibrium one (4.0515 Å) of the AlSi10Mg alloy [31]. Additionally, Si reflections barely stand out from the background in Fig. 3e, suggesting a reduced amount of crystalline Si with a nanometric size. Indeed, a weigh fraction of Si of ~8.0 ± 0.3% was calculated by the Rietveld method. From the mass balance of the alloy with a calculated amount of Si of 9.6 wt.% by optical emission spectroscopy, the residual Si retained in solid solution in the α-Al phase was estimated as ~1.85 wt.%.

Microstructural features were quantitatively evaluated by image analysis to confirm the negligible effect of VED, and results are reported in Fig. 3f. The logarithmic Y-axis shows that the size of microstructural features extends over two orders of magnitude, but it does not appreciably change with VED. The mean width of elongated grains and cells is 14 ± 2 μm and 1 ± 0.05 μm, respectively. The mean ED and volumetric fraction of Si precipitates are 72 ± 8 nm and 2.2 ± 0.2 %, respectively, similarly to [32].

3.3 Mechanical properties and fracture surfaces

Figure 4 depicts the relationship between VED and Brinell hardness, which mirrors the one in Fig. 2f. As the energy density increases, porosity significantly raises and negatively affects hardness. Data in Fig. 4 are reported into two series (filled and open markers) as a function of *h*.

Both series show that, for a given *h*, hardness decreases with a reduction of *v*. Similarly, at constant *v*, hardness is lower using a smaller *h*. As in Fig.2f, the separate effect of deposition parameters can be described incorporating them in a single energy parameter, that is in a univocal relationship with the hardness.

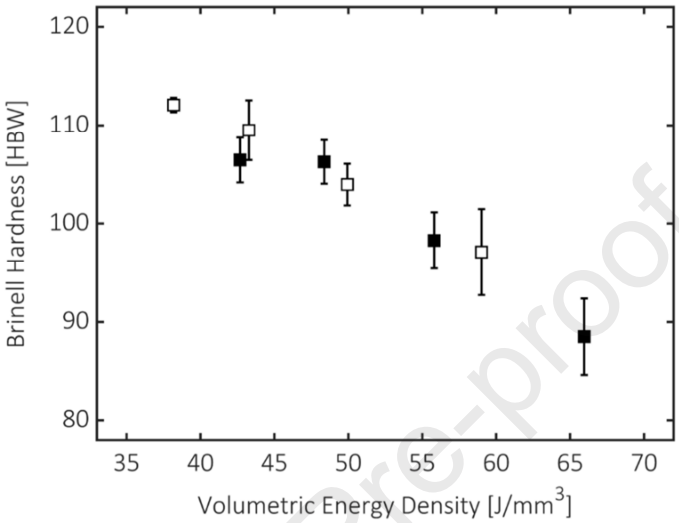

Figure 4. Brinell hardness of samples produced with different VED values. Filled and open markers correspond to hatch spacing h and 1.12h, respectively. Standard deviation is reported as error bar.

Figure 5 depicts the engineering stress-strain curves of each investigated condition. Specimens produced with low *v* and *h* (v-h, v-1.12h), and thus with the highest energy density, display the worst mechanical properties. As the energy density reduces, both strength and ductility progressively raise, reaching the outstanding tensile strength of ~500-550 MPa, and a reasonable elongation of ~6%, at the highest values of *v* and *h* (1.55v-h, 1.55v-1.12h). Similar performances were achieved just for specifically designed high-strength Al alloys [7,8,32], while the resistance of the AlSi10Mg alloy ranges between 350-450 MPa in the literature [10,16,20,27].

Despite the different final properties, all the stress-strain curves display a similar shape. The applied stress reaches a maximum, and then the alloy abruptly fails during the strain-hardening stage, without any evidence of stress reduction. The necking stage is absent, and thus the alloy fails

before the potential UTS is reached. True stress (σ) and strain hardening rate (Θ) are plotted as a function of the true strain (ε) in the insets in Fig. 5 for each investigated condition to assess such behaviour furtherly. According to Considère's criterion [33], necking starts when $\Theta = d\sigma/d\varepsilon = \sigma$, at the intersection of σ and Θ curves. However, insets in Fig. 5 show that, in most cases, such a condition is not satisfied, even if σ and Θ values at failure are generally quite close. Similar behaviour is often reported in the literature of additively manufactured parts [21,34,35], and it is ascribed to the existence of a high density of microstructural defects, like tangled dislocations, residual stresses and sub-micrometric pores. However, in the current study, abrupt failure is more likely determined by keyhole pores, which overtake the effect of features mentioned above.

Journal Pre-proof

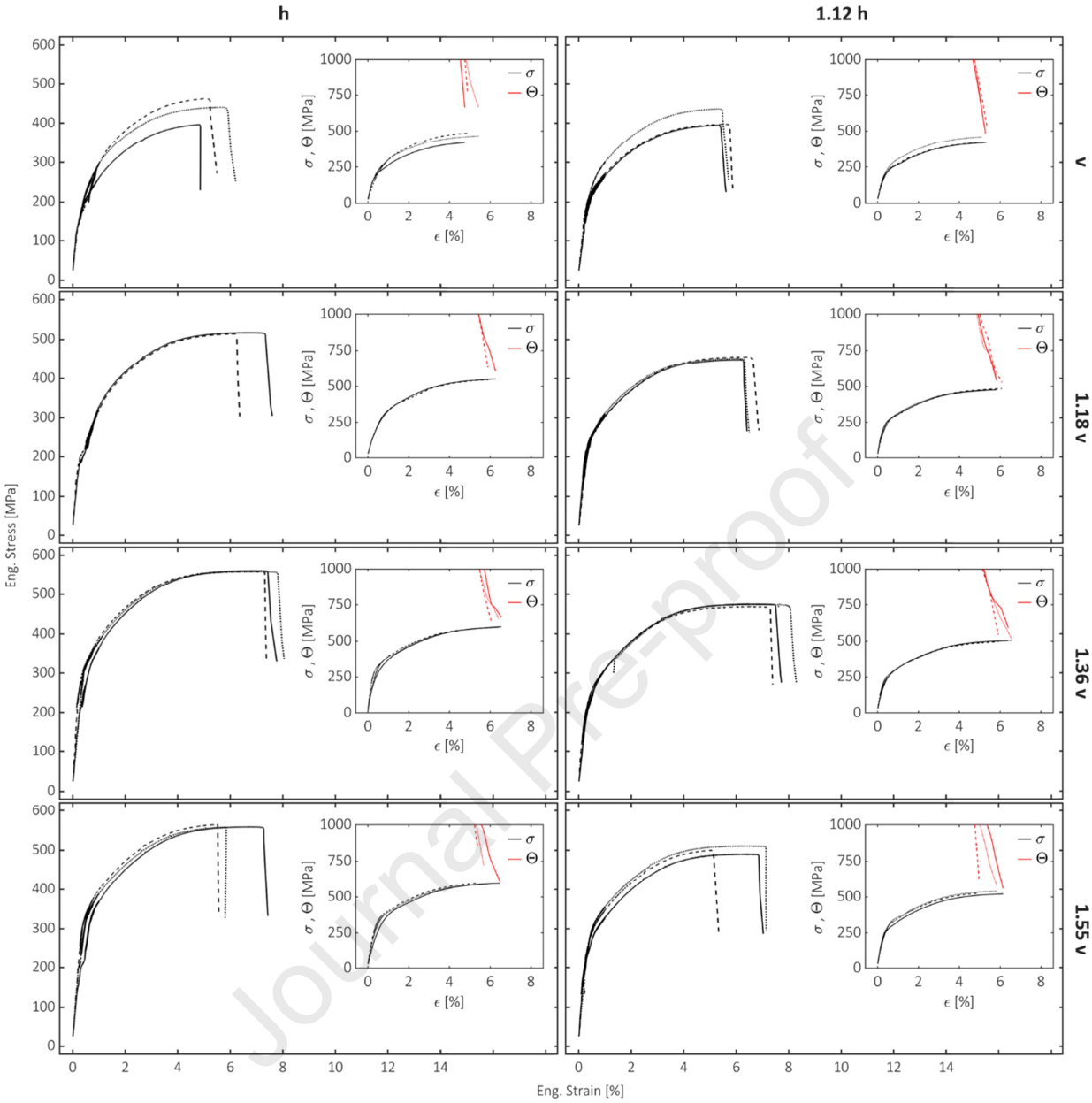

Figure 5. Engineering stress-strain curves of samples produced with different VED values. Insets depict the corresponding true stress-true strain (σ) and strain hardening-true strain (Θ) curves.

Figure 6 reports tensile parameters as a function of investigated *v*-*h* combinations and the corresponding VED. A maximum value of 78 ± 9 GPa of elastic modulus (E) is reached at the lowest energy density of 38 J/mm^3. Similar E values were reported for a fully dense AlSi10Mg alloy [27]. The elastic modulus falls almost linearly to 57 ± 6 GPa as the VED increases to the maximum value of 66 J/mm^3. Other tensile parameters, yield strength (YS), ultimate tensile strength (UTS)

and elongation at failure (E_f), also approximately decrease with the energy density, and each one is reduced by ~20-25% of its maximum value. YS falls from 300-320 MPa down to 220-240 MPa and UTS from 500-550 MPa to 410-430 MPa, whereas E_f decreases from 6-6.5% to ~5%.

Figure 6 shows that, conversely to elastic modulus and hardness, specimens produced at constant *v* with the lowest *h* (h) exhibit better performances than their counterparts (1.12 h). UTS more clearly shows such an effect, because of the high deviation that YS and E_f suffer. A further comparison concerns samples produced with very close VED values. The energy density of 1.55v-h and 1.36v-1.12h specimens is almost the same (42 and 43 J/mm^3 respectively), but the former display better mechanical properties as compared to the latter. The same observation rules for the 1.36v-h and 1.18v-1.12h specimens, realised with a VED of 48 and 50 J/mm^3, respectively.

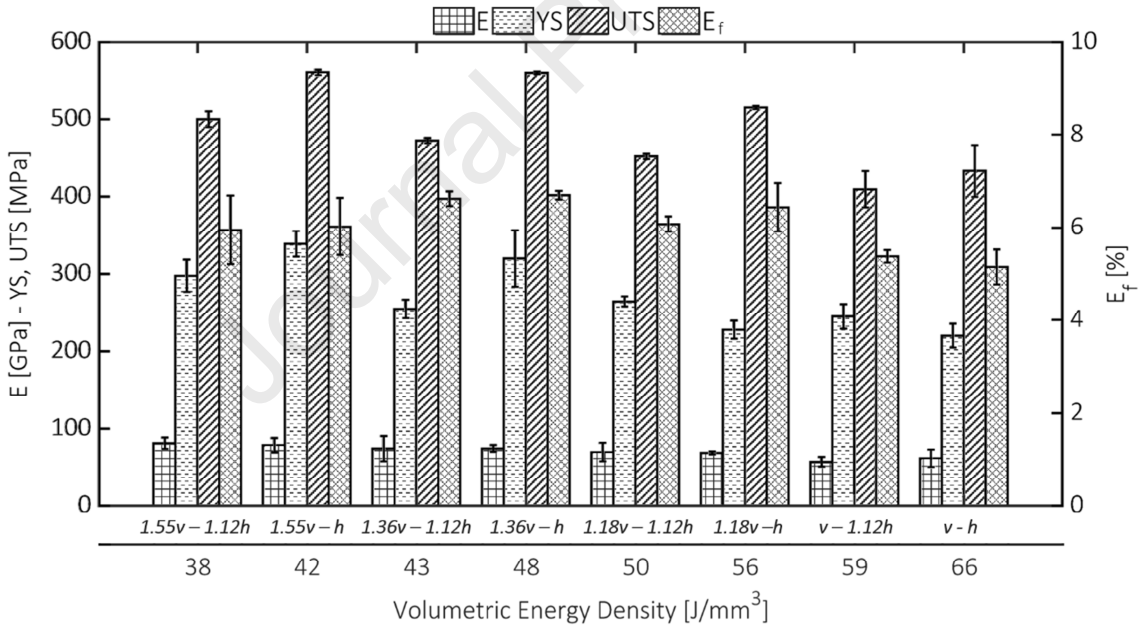

Figure 6. Tensile parameters of samples produced with different VED values. Standard deviation is reported as error bar.

Results of image analysis in Fig. 1f showed that the porosity increases as VED raises. A complementary analysis was performed on the fracture surface of tensile specimens, and results

are reported in Fig. 7. Probability histograms depict the size distribution of pores on the fracture surfaces and confirm results in Fig. 1d: at low VED, most of the pores are a few tens of μm wide, with the probability of finding large pores (ED > 100 μm) being almost zero. At intermediate VED, the appearance of pores several tens of μm wide became more and more probable. These latter are the most probable at high VED, together with large pores ranging between 100-200 μm.

Journal Pre-proof

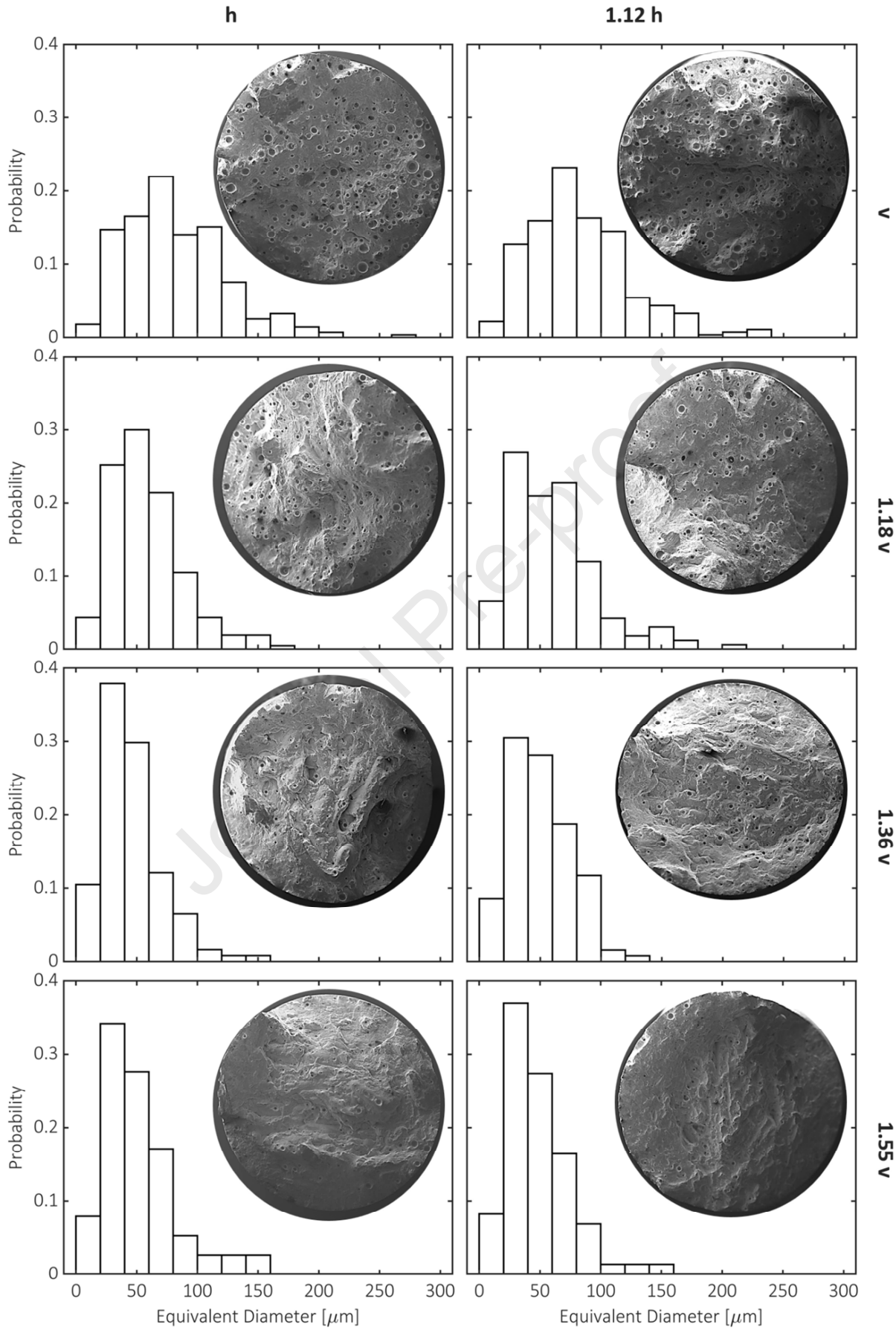

Journal Pre-proof

Journal Pre-proof

Figure 7. ED probability histograms of pores on the fracture surfaces of samples produced with different deposition parameters.

A comparison between Fig. 7 and Fig. 1d shows that the size range of pores on fracture surfaces and metallographic sections closely correspond at each VED value. This result suggests that tensile specimens experienced limited plasticity before failure, with pores being otherwise somewhat deformed. In turn, this observation matches the tensile behaviour and premature failure shown in Fig. 6.

A more in-depth analysis of the fracture surfaces is proposed in Fig. 8, considering specimens produced with the lowest (Figs. 8a-b) and highest (Figs. 8c-d) energy densities, respectively. Samples processed with a low VED show a limited number of small pores and several elongated features, these latter marked by a dashed circular line in Fig. 8a. Figure 8b clarifies these features to be traces of tracks produced by the laser scan. Other works report the coarse and heat-affected microstructure of melt pool boundaries to be a weak microstructural feature and an easy fracture path [36], which explains the presence of scan tracks on the fracture surface. The inset of Fig. 8b points out that, on a smaller scale, the fracture surface is made up of fine dimples.

Journal Pre-proof

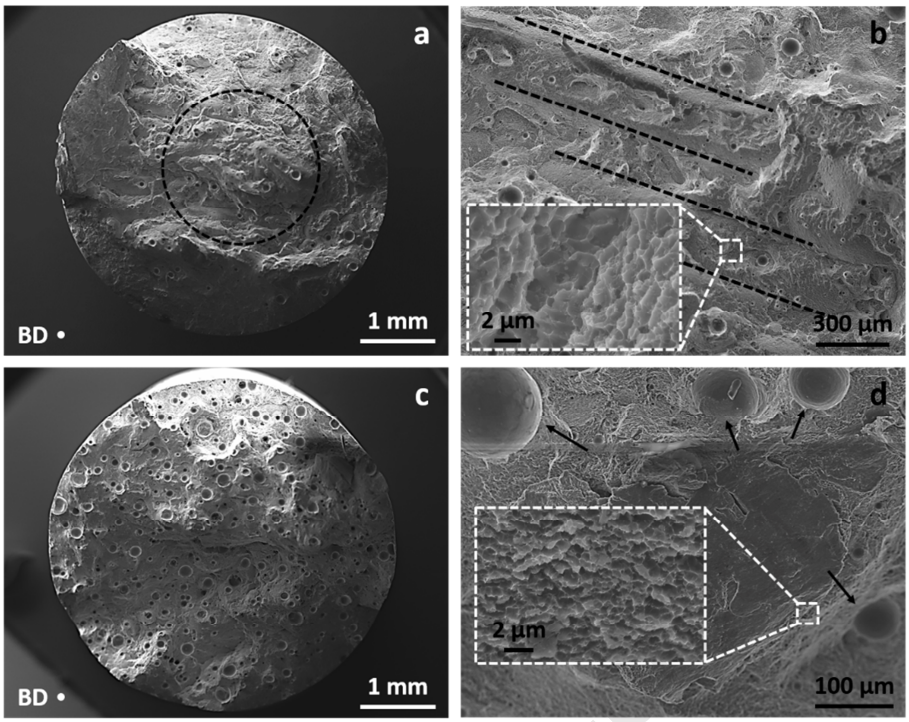

Figure 8. Fracture surfaces of samples produced with (a-b) low and (c-d) high energy density. (a) Macro-fracture, the circled area highlights elongated features. (b) Particular of the scan tracks marked with dotted lines; the inset depicts fine dimples. (c) Macro-fracture. (d) Particular of coarse pores pointed by black arrows; the inset depicts fine dimples. In (a-c), the dot on the bottom left corner highlights the building direction (BD).

Samples produced with a high energy density show copious coarse pores on the surface (Fig. 8c). Conversely to Figs. 8a-b, traces of the scan tracks are not distinguishable. Pores represent a weaker feature than melt pool boundaries, and they mainly guide the fracture at a macroscopic level, making the scan tracks no longer detectable. On the contrary, the inset of Fig. 8d depicts small dimples as in Fig. 8b, elucidating a similar fracture mechanism at the microscale. The fracture behaviour at the microscale was deepened analysing and comparing the spacing of fine dimples in Figs. 8b-d and smallest microstructural features, Al cells and Si precipitates, in Figs. 3c-d. Results were averaged among all the investigated conditions since no significant differences of microstructural features were detected (Fig. 3f). From Fig. 3f, the spacing of Al cells matches their

width, and it is ~1 μm, whereas the mutual distance of Si precipitates was measured as ~210 ± 75 nm. For the ease of analysis, no distinction was made between globular and acicular precipitates, which accounts for the scatter of measurements. The mean spacing of dimples on the fracture surfaces was measured as ~270 ± 65 nm, which more closely resembles that of Si particles rather than Al cells, suggesting the formers to mainly rule the deformation behaviour at the microscale.

4. Discussion

4.1 Process parameters, VED and porosity

OM observations in Figs. 2a-b-c highlight that, a decrease of either v or h promotes the formation of large round pores up to 100-200 μm wide. Consequently, the relative density falls from 99% of the almost dense material to ~96%, as reported in Fig. 2f.

The AM process of Al components could suffer from different kinds of porosity, usually classified in lack-of-fusion and keyhole porosity. The former depends on the incomplete powder melting, caused by a poor overlap of melting pools or by insufficient laser power. Due to their inherent nature, lack-of-fusion pores are usually very irregularly-shaped [15], and do not fit with the current OM observation. Conversely, the keyhole porosity is determined by an excess of energy that the laser imparts to the powder. The resulting overheating, metal vaporisation and recoil pressure, drive the melt pool surface deep into the material to form a keyhole depression. Due to its inherent instability, such depression easily collapses and traps the inert shielding gas, giving rise to the pore formation within the substrate. The resulting pore is almost spherical and located at the bottom of the melt pool [13,14]. Accordingly, the circularity of pores in Figs. 2a-b-c, and their location in the low part of melt pools, strongly suggest them to be keyhole pores. Additionally, Fig. 2e shows that the depth-to-width ratio of all measured melt pools ranges

between 0.5 and 1, regardless of VED, confirming that samples were produced under a keyhole heat conduction mode, following previously published works [29,30].

4.2 Process parameters, VED and microstructural features

SEM observation shows the hierarchical microstructure of the L-PBF produced AlSi10Mg alloy (Fig. 3) [3,4,6]. Columnar grains grow radially and epitaxially through the melt pools (Fig. 3b), with their cubic {100} orientation along the building direction (Fig. 3e). Epitaxy and strong crystallographic texture can be ascribed to the strong thermal gradients that develop during the L-PBF process [3]. Inside the grains, a fibrous Si network surrounds micrometric Al cellular dendrites (Fig. 3c). An estimated high cooling rate of ~10^3-10^5 K/s [32] accounts for their micrometric size, and determines the fibrous morphology of Si, accordingly to the quench modification phenomenon [37]. The high cooling rate also extends the solubility of Si inside the Al phase during the solidification. XRD analyses (Fig. 3e) confirm such a statement measuring ~1.85 wt.% of Si retained in solid solution [5]. As the cooling proceeds, the solubility of Si falls and it is partially ejected from the Al matrix to form nanometric features (Fig. 3d), even if they also likely precipitate and coarsen due to the heating produced by neighbouring laser scans.

Besides the peculiar microstructure, a change in the deposition parameters as reported in Tab. 1 does not modify the microstructural features significantly (Fig. 3f). Size and morphology of these latter depend on thermal gradient G and growth rate R. The G/R ratio determines the stability of the solid/liquid front and the resulting solidification mode, while the G·R product, i.e. the cooling rate, rules the final size of the microstructure. In the steady-state conditions:

$$R = v \cdot \cos\vartheta \quad (4)$$

where v is the scan speed, and ϑ is the angle between the scan direction of the laser and the growth direction of the solidifying material [3]. G depends on the alloy properties and the energy

imparted to the material, thus on building parameters, like lase power P and scan speed v. However, numerical simulations proved that P is a slightly influencing variable, while v has a neglecting effect [38]. Therefore, a constant G value of ~10^6 K/m is often reported [39]. The limited h difference of 12% employed in this work reasonably just slightly modifies the total heat input from neighbouring scan tracks. Therefore, in the following discussion, its effect on microstructural features will be neglected, with G/R and G·R mainly depending on v of the moving source.

Increasing v and thus reducing G/R, planar, cellular and dendritic structures are progressively expected. Nevertheless, the Al phase of samples produced at different v always exhibits a cellular structure (Fig. 3c-f). Likely, the high G prevents the increasing v from changing the solidification mode. Similarly, the size of microstructural features does not change significantly among the investigated samples (Fig. 3f), despite its dependence on the cooling rate according to $G \cdot R = G \cdot v \cdot cos\vartheta$. A typical relationship between cell size and cooling rate is:

$$\lambda = a \cdot \left(\dot{T}\right)^{-n} = a \cdot (G \cdot R)^{-n} \quad (5)$$

where λ [μm] is the cell size for cellular growth, a [μm·s/K] is a proportional constant, $\dot{T}$ [K/s] is the cooling rate, and n is a dimensionless exponent ranging between 0.32-0.38, often assumed as 0.33 [40]. From Tab. 1, the maximum v variation in this work is 55% for samples produced with v and 1.55v. The maximum expected size difference of cells is ~13% applying equation (5), which reasonably falls in the experimental uncertainty of size measurement. Similar considerations also apply to other microstructural features, like elongated grains and Si precipitates, and explain why no significant differences were found among the investigated samples (Fig. 3f).

Since similar microstructural features were obtained as the deposition parameters change, their contribution to mechanical performance is more or less constant. Conversely, small variations of v and h remarkably affect density (Fig. 2f). As a consequence, both hardness (Fig. 4) and tensile

properties (Fig. 5 and Fig. 6) decrease as VED increases. However, some relevant considerations hide behind this somewhat trivial result, as will be elucidated in the following discussion.

4.3 Limitations of VED as a reliable design parameter

In this work, a VED of ~40 J/mm^3 is suitable to minimise the porosity level. Additionally, the density reduction with any variation of v and h is fully described by VED (Fig. 2f), which stems from the strong dependence of the keyhole phenomenon on the energy density. In this light, the energy density-based approach seems a valuable tool to define a proper process window of deposition parameters. However, Fig. 9a highlights a very different situation. According to literature data, the relative density of the AlSi10Mg alloy in a VED range of 30-110 J/mm^3 uniformly distributes between 98-100%. Conversely, we found that porosity steeply increases as VED raises from 40 to 70 J/mm^3 (red markers in Fig. 9a). Even if not available, any additional increment beyond 70 J/mm^3 would further deteriorate density. Thus, a very different amount of porosity could be achieved at the same VED value, which severely limits its applicability to determine a suitable combination of deposition parameters. Such an outcome stems from the extreme simplicity of equation (1): it comprehends just a few of the assessable process parameters and does not account for material properties and physical events that characterise the dynamic of solidifying melt pools. Therefore, a mere energy density-based approach cannot capture the complexity of the AM process, with the effect of individual deposition parameters that cannot be neglected.

Fig. 6 shows that tensile properties roughly decrease as VED increases, according to the raised amount of porosity. However, specimens produced with an almost equal VED exhibit a very close porosity but a different mechanical response. For instance, comparing 1.55v-h and 1.36v-1.12h specimens (42 and 43 J/mm^3, respectively) and 1.36v-h and 1.18v-1.12h specimens (48 and 50

J/mm³, respectively), porosity differs less than 0.2%, whereas UTS differs ~100 MPa. In both cases, the specimen realised with the lowest *h* shows superior mechanical properties, in agreement with [41]. Such an effect is ascribed to the higher geometrical overlapping between adjacent tracks, which provides a better material consolidation. This finding suggests that process parameters exert additional effects, besides energy transfer, not taken into account by the energy density-based approach. For industrial purposes, this limitation possibly leads to define the best combination of deposition parameters erroneously.

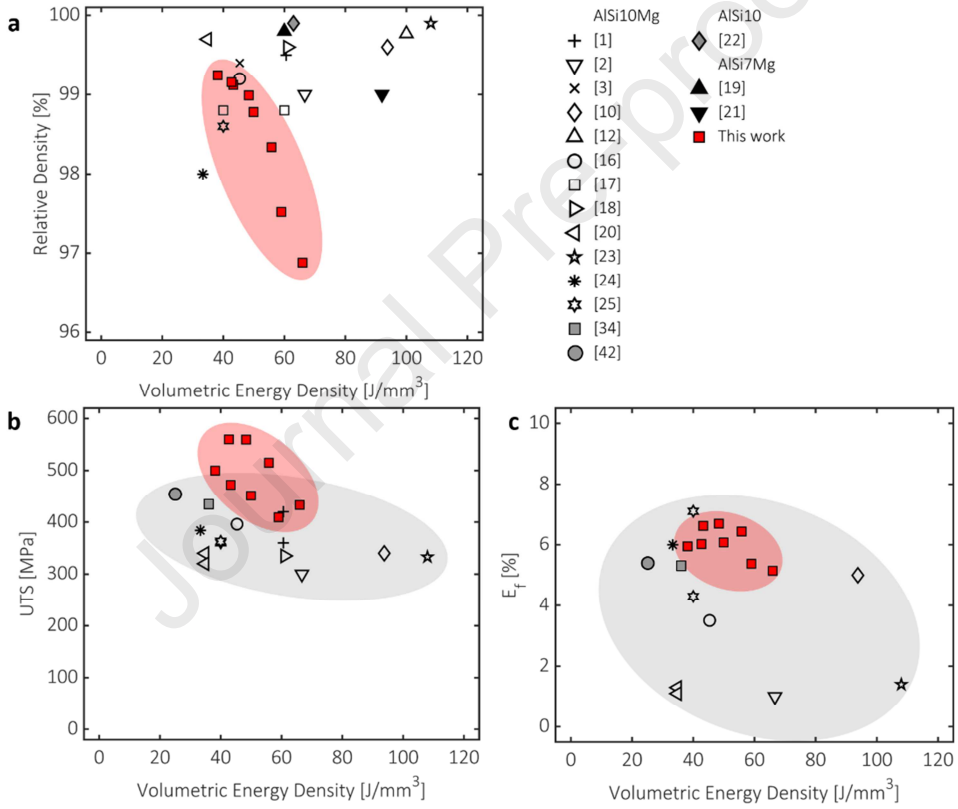

Figure 9. Comparison of literature data of the AlSi10Mg alloy (grey clouds) with results from this work (red clouds) as a function of VED. (a) Relative density. (b) UTS. (c) E_f.

Figures 9b-c furtherly compare present tensile results with available literature data. In the 30-110 J/mm³ range of VED, UTS of the AlSi10Mg alloy ranges between 300-400 MPa, with few exceptions up to 450 MPa [34,42], whereas E_f ranges between 1-6%. Conversely, our specimens

exhibit a systematically higher UTS (400-550 MPa), preserving a considerable E_f (5-6.5%). These latter values are quite surprising considering the significant porosity of our samples (up to 3.5%) and their vertical building orientation. Vertically built specimens generally show worse tensile properties, particularly E_f, than horizontally built ones [2,10,20], with the corresponding values that occupy the bottom part of Fig. 9c.

The outstanding mechanical properties reached in this work could be ascribed to the hierarchical structure of the AlSi10Mg alloy. It exploits all the strengthening mechanisms of metallic materials, namely internal friction, Hall-Petch, Orowan, Taylor, solid solution and load-bearing mechanisms, with the corresponding relationships reported, in this order, as follows:

$$YS_{est.} = [\sigma_0] + \left[\frac{k}{\sqrt{d_{cell}}} + \frac{k}{\sqrt{d_{grain}}}\right] + \left[\frac{\varphi G b}{d_{Si.particle}}\left(\frac{6V_{Si.particle}}{\pi}\right)^{1/3}\right] + [\beta M G b\sqrt{\rho_d}] + [HC_{Si}{}^{N}] + [1.5\sigma_i V_{Si.eutectic}] \quad (6)$$

where σ_0 is the internal friction (72 MPa, [43]), k (50 MPa·μm$^{0.5}$, [32]), φ (~2, [32]), β (0.16, [44]), H (~13 MPa·at.%$^{-1}$, [45]), N (1, [45]) are a material constants, d_{cell} (1 ± 0.05 μm) and d_{grain} (14 ± 2 μm) are widths of Al cells and elongated grains, G (27000 MPa) and b (0.286 nm) are shear modulus and Burger vector of the Al phase, $d_{Si.particle}$ (72 ± 8 nm) and $V_{Si.particle}$ (0.022 ± 0.002) are size and volumetric fraction of Si precipitates, M is the Taylor factor of FCC crystals (3.06, [34]), ρ_d is the dislocation density ($3.05 \cdot 10^{14}$ m^{-2}, [46]), C_{Si} is the solid solution Si (~1.8 ± 0.3 at.%), σ_i is the bonding strength of the Al/Si interface (240 MPa, [47]), and $V_{Si.eutectic}$ is the volumetric fraction of eutectic Si. This latter value is calculated as the difference between total crystalline Si (0.091 ± 0.004, from XRD results) and Si precipitates. Applying (6), individual reinforcement contributions are calculated as 72, 63, 75, 66, 23 and 25 MPa, which shows the relevant role of Al cells and Si precipitates to the alloy strength. The estimated yield strength $YS_{est.}$ is 325 ± 10 MPa, which very well matches YS of 1.55v-h and 1.55v-1.12h samples, and thus correspond to the strength of the almost dense material. In this light, the contribution of porosity Φ [%] to strength loss can be

estimated as ~40 MPa· Φ^{-1} from data in Fig. 6. The harmful effect of pores is much pronounced compared to the strengthening effect of microstructural features, which suggest the importance of using optimised process parameters.

Preservation of a high E_f despite the increasing porosity stems from the microscale fracture behaviour. In dense samples, MPBs represent the weakest fracture path (Figs. 8a-b), whereas keyhole pores substitute them in porous specimens (Figs. 8d-e). Despite such difference at the macroscale, similar fine dimples form during the deformation stage at the microscale (insets of Figs. 8b-d). Quantitative analyses show that dimples are ~270 nm spaced similarly to Si precipitates (~210 nm), from which they likely nucleate and grow. During the deformation stage, Si precipitates provide plenty of additional sites for strain localisation other than large keyhole pores, avoiding these latter to cause excessive damage accumulation and enhancing a ductile behaviour [48]. As a consequence, E_f limitedly suffers from the increased porosity, and moderately falls from 6.5% to 5%. A further reason for the relevant ductility of our specimens is the lack of defects other than keyhole pores, like oxides, unmelted powder particles and shrinkage voids, as stated in section 3.1. Such features are sometimes reported in additively manufactured Al alloys [10,11,20] and would remarkably contribute to tensile properties reduction. It is worth to note that, despite the relevant ductility, tensile curves in Fig. 5 show that all samples prematurely fail before the necking stage. Keyhole pores and possible additional defects, such as densely tangled dislocations and residual stresses, likely explain such behaviour.

The analysis reported above shows that VED is not a reliable parameter to estimate tensile properties of the additively manufactured AlSi10Mg alloy. The energy density-based approach accounts for the effect of deposition parameters mainly on porosity but lacks in considering their impact on the microstructural features which, as here demonstrated, significantly impact on the final mechanical performance. Our work highlights that the use of VED, as currently defined, to

determine the proper combination of process parameters would not necessarily guarantee the optimum choice. Hence, although it could help in determining an adequate range of process parameters, it cannot be intended as a reliable design parameter.

5. Concluding remarks

In the present work, different combinations of building parameters were employed to realise AlSi10Mg alloy specimens by DMLS technology within a specific VED range, based on a literature survey. Metallurgical and mechanical characterisations were conducted to investigate the effect of VED and deposition parameters on porosity, microstructural features and tensile properties of the alloy. Results were compared with literature data to highlight some relevant limitations of the energy density-based approach. The following conclusions can be drawn:

- A limited variation of process parameters remarkably affects the porosity of the alloy but has a negligible effect on the microstructural features. This is an advantage where the process is to be optimised for defect reduction or productivity maximisation.
- The VED range suggested in the literature does not necessarily lead to fully dense parts, with the present specimens showing up to 3.5% of porosity. Very different amount of porosity could be achieved with the same VED value. The simplified energy density-based approach just roughly estimates the energy imparted to powder bed and cannot predict the final density of additively manufactured components. Besides considering just a few parameters, it lacks in assessing the effect of individual deposition parameters on the dynamic of the melt pool, which significantly affects porosity.
- The almost dense material shows outstanding tensile properties. The strengthening contribution of each microstructural feature was estimated to assess its individual effect on material strength. Results well match experimental tensile properties and show that Al cells

and Si precipitates provide the primary reinforcement. However, even a limited porosity dramatically reduces material strength and overtakes the contribution of microstructure.

- At equal or similar VED, specimens produced with a lower *h* show better tensile properties. Additionally, our specimens exhibit systematically higher tensile performance as compared to literature data. VED just roughly estimates the effect of deposition parameters on the amount of energy imparted to the powder bed. Conversely, it lacks in assessing their effect on the microstructural features and fails in predicting the final properties of the alloy.
- As currently defined, the use of VED guarantees neither the selection of suitable deposition parameters nor the optimisation of material properties. Hence, it cannot be intended as a reliable design parameter.

Acknowledgements

The authors are grateful to AMT S.r.l. (Camposanto, Italy) and in particular to Ing. Manuel Bertani for the design of the process parameters, specimens manufacturing and tensile tests.

Funding

This work was partially funded by the University Found for the Scientific Research (FAR) 2019 of the University of Ferrara (Italy).

Data availability

The data that support the findings of this study are available from the corresponding author on reasonable request.

References:

Journal Pre-proof

Journal Pre-proof

[1] D. Buchbinder, H. Schleifenbaum, S. Heidrich, W. Meiners, J. Bültmann, High power Selective Laser Melting (HP SLM) of aluminum parts, Phys. Procedia. 12 (2011) 271–278. https://doi.org/10.1016/j.phpro.2011.03.035.

[2] E. Brandl, U. Heckenberger, V. Holzinger, D. Buchbinder, Additive manufactured AlSi10Mg samples using Selective Laser Melting (SLM): Microstructure, high cycle fatigue, and fracture behavior, Mater. Des. 34 (2012) 159–169. https://doi.org/10.1016/j.matdes.2011.07.067.

[3] L. Thijs, K. Kempen, J.P. Kruth, J. Van Humbeeck, Fine-structured aluminium products with controllable texture by selective laser melting of pre-alloyed AlSi10Mg powder, Acta Mater. 61 (2013) 1809–1819. https://doi.org/10.1016/j.actamat.2012.11.052.

[4] J. Wu, X.Q. Wang, W. Wang, M.M. Attallah, M.H. Loretto, Microstructure and strength of selectively laser melted AlSi10Mg, Acta Mater. 117 (2016) 311–320. https://doi.org/10.1016/j.actamat.2016.07.012.

[5] T. Maeshima, K. Oh-ishi, Solute clustering and supersaturated solid solution of AlSi10Mg alloy fabricated by selective laser melting, Heliyon. 5 (2019) e01186. https://doi.org/10.1016/j.heliyon.2019.e01186.

[6] X. Liu, C. Zhao, X. Zhou, Z. Shen, W. Liu, Microstructure of selective laser melted AlSi10Mg alloy, Mater. Des. 168 (2019) 107677. https://doi.org/10.1016/j.matdes.2019.107677.

[7] R. Casati, M. Coduri, M. Riccio, A. Rizzi, M. Vedani, Development of a high strength Al–Zn–Si–Mg–Cu alloy for selective laser melting, J. Alloys Compd. 801 (2019) 243–253. https://doi.org/10.1016/j.jallcom.2019.06.123.

[8] Q. Jia, P. Rometsch, S. Cao, K. Zhang, X. Wu, Towards a high strength aluminium alloy development methodology for selective laser melting, Mater. Des. 174 (2019) 107775. https://doi.org/10.1016/j.matdes.2019.107775.

[9] J.R. Croteau, S. Griffiths, M.D. Rossell, C. Leinenbach, C. Kenel, V. Jansen, D.N. Seidman, D.C. Dunand, N.Q. Vo, Microstructure and mechanical properties of Al-Mg-Zr alloys processed by

Journal Pre-proof

selective laser melting, Acta Mater. 153 (2018) 35–44. https://doi.org/10.1016/j.actamat.2018.04.053.

[10] P. Wei, Z. Wei, Z. Chen, J. Du, Y. He, J. Li, Y. Zhou, The AlSi10Mg samples produced by selective laser melting: single track, densification, microstructure and mechanical behavior, Appl. Surf. Sci. 408 (2017) 38–50. https://doi.org/10.1016/j.apsusc.2017.02.215.

[11] S. Siddique, M. Imran, E. Wycisk, C. Emmelmann, F. Walther, Influence of process-induced microstructure and imperfections on mechanical properties of AlSi12 processed by selective laser melting, J. Mater. Process. Technol. 221 (2015) 205–213. https://doi.org/10.1016/j.jmatprotec.2015.02.023.

[12] N.T. Aboulkhair, N.M. Everitt, I. Ashcroft, C. Tuck, Reducing porosity in AlSi10Mg parts processed by selective laser melting, Addit. Manuf. 1 (2014) 77–86. https://doi.org/10.1016/j.addma.2014.08.001.

[13] A.A. Martin, N.P. Calta, S.A. Khairallah, J. Wang, P.J. Depond, A.Y. Fong, V. Thampy, G.M. Guss, A.M. Kiss, K.H. Stone, C.J. Tassone, J. Nelson Weker, M.F. Toney, T. van Buuren, M.J. Matthews, Dynamics of pore formation during laser powder bed fusion additive manufacturing, Nat. Commun. 10 (2019). https://doi.org/10.1038/s41467-019-10009-2.

[14] M. Bayat, A. Thanki, S. Mohanty, A. Witvrouw, S. Yang, J. Thorborg, N.S. Tiedje, J.H. Hattel, Keyhole-induced porosities in Laser-based Powder Bed Fusion (L-PBF) of Ti6Al4V: High-fidelity modelling and experimental validation, Addit. Manuf. 30 (2019) 100835. https://doi.org/10.1016/j.addma.2019.100835.

[15] G. Kasperovich, J. Haubrich, J. Gussone, G. Requena, Correlation between porosity and processing parameters in TiAl6V4 produced by selective laser melting, Mater. Des. 105 (2016) 160–170. https://doi.org/10.1016/j.matdes.2016.09.040.

[16] K. Kempen, L. Thijs, J. Van Humbeeck, J.P. Kruth, Processing AlSi10Mg by selective laser melting: Parameter optimisation and material characterisation, Mater. Sci. Technol. (United Kingdom). 31 (2015) 917–923. https://doi.org/10.1179/1743284714Y.0000000702.

Journal Pre-proof

[17] M. Krishnan, E. Atzeni, R. Canali, F. Calignano, D. Manfredi, E.P. Ambrosio, L. Iuliano, On the effect of process parameters on properties of AlSi10Mg parts produced by DMLS, Rapid Prototyp. J. 20 (2014) 449–458. https://doi.org/10.1108/RPJ-03-2013-0028.

[18] R.K. Shah, P.P. Dey, Process parameter optimization of dmls process to produce AlSi10Mg components, J. Phys. Conf. Ser. 1240 (2019) 1–9. https://doi.org/10.1088/1742-6596/1240/1/012011.

[19] T. Kimura, T. Nakamoto, Microstructures and mechanical properties of A356 (AlSi7Mg0.3) aluminum alloy fabricated by selective laser melting, Mater. Des. 89 (2016) 1294–1301. https://doi.org/10.1016/j.matdes.2015.10.065.

[20] N. Read, W. Wang, K. Essa, M.M. Attallah, Selective laser melting of AlSi10Mg alloy: Process optimisation and mechanical properties development, Mater. Des. 65 (2015) 417–424. https://doi.org/10.1016/j.matdes.2014.09.044.

[21] N.T. Aboulkhair, I. Maskery, C. Tuck, I. Ashcroft, N.M. Everitt, The microstructure and mechanical properties of selectively laser melted AlSi10Mg: The effect of a conventional T6-like heat treatment, Mater. Sci. Eng. A. 667 (2016) 139–146. https://doi.org/10.1016/j.msea.2016.04.092.

[22] N.E. Uzan, R. Shneck, O. Yeheskel, N. Frage, Fatigue of AlSi10Mg specimens fabricated by additive manufacturing selective laser melting (AM-SLM), Mater. Sci. Eng. A. 704 (2017) 229–237. https://doi.org/10.1016/j.msea.2017.08.027.

[23] Z.H. Xiong, S.L. Liu, S.F. Li, Y. Shi, Y.F. Yang, R.D.K. Misra, Role of melt pool boundary condition in determining the mechanical properties of selective laser melting AlSi10Mg alloy, Mater. Sci. Eng. A. 740–741 (2019) 148–156. https://doi.org/10.1016/j.msea.2018.10.083.

[24] Y. Bai, Y. Yang, Z. Xiao, M. Zhang, D. Wang, Process optimization and mechanical property evolution of AlSiMg0.75 by selective laser melting, Mater. Des. 140 (2018) 257–266. https://doi.org/10.1016/j.matdes.2017.11.045.

[25] T. Kimura, T. Nakamoto, M. Mizuno, H. Araki, Effect of silicon content on densification, mechanical

and thermal properties of Al-xSi binary alloys fabricated using selective laser melting, Mater. Sci. Eng. A. 682 (2017) 593–602. https://doi.org/10.1016/j.msea.2016.11.059.

[26] W.H. Kan, Y. Nadot, M. Foley, L. Ridosz, G. Proust, J.M. Cairney, Factors that affect the properties of additively-manufactured AlSi10Mg: Porosity versus microstructure, Addit. Manuf. 29 (2019) 100805. https://doi.org/10.1016/j.addma.2019.100805.

[27] Material Data Sheet: EOS Aluminium AlSi10Mg, 2014. http://gpiprototype.com/images/PDF/EOS_Aluminium_AlSi10Mg_en.pdf.

[28] L. Lutterotti, H.R. Wenk, S. Matthies, MAUD (Material Analysis Using Diffraction): a user friendly Java program for Rietveld Texture Analysis and more, in: ICOTOM-12., 1999: pp. 1599–1604.

[29] W.E. King, H.D. Barth, V.M. Castillo, G.F. Gallegos, J.W. Gibbs, D.E. Hahn, C. Kamath, A.M. Rubenchik, Observation of keyhole-mode laser melting in laser powder-bed fusion additive manufacturing, J. Mater. Process. Technol. 214 (2014) 2915–2925. https://doi.org/10.1016/j.jmatprotec.2014.06.005.

[30] N.T. Aboulkhair, I. Maskery, C. Tuck, I. Ashcroft, N.M. Everitt, On the formation of AlSi10Mg single tracks and layers in selective laser melting: Microstructure and nano-mechanical properties, J. Mater. Process. Technol. 230 (2016) 88–98. https://doi.org/10.1016/j.jmatprotec.2015.11.016.

[31] S. Marola, D. Manfredi, G. Fiore, M.G. Poletti, M. Lombardi, P. Fino, L. Battezzati, A comparison of Selective Laser Melting with bulk rapid solidification of AlSi10Mg alloy, J. Alloys Compd. 742 (2018) 271–279. https://doi.org/10.1016/j.jallcom.2018.01.309.

[32] X.P. Li, G. Ji, Z. Chen, A. Addad, Y. Wu, H.W. Wang, J. Vleugels, J. Van Humbeeck, J.P. Kruth, Selective laser melting of nano-TiB2decorated AlSi10Mg alloy with high fracture strength and ductility, Acta Mater. 129 (2017) 183–193. https://doi.org/10.1016/j.actamat.2017.02.062.

[33] G.E. Dieter, D.J. Bacon, Mechanical Metallurgy, 1986.

[34] B. Chen, S.K. Moon, X. Yao, G. Bi, J. Shen, J. Umeda, K. Kondoh, Strength and strain hardening of a

Journal Pre-proof

selective laser melted AlSi10Mg alloy, Scr. Mater. 141 (2017) 45–49. https://doi.org/10.1016/j.scriptamat.2017.07.025.

[35] Z. Wang, M. Xie, Y. Li, W. Zhang, C. Yang, L. Kollo, J. Eckert, K.G. Prashanth, Premature failure of an additively manufactured material, NPG Asia Mater. 12 (2020). https://doi.org/10.1038/s41427-020-0212-0.

[36] I. Rosenthal, A. Stern, N. Frage, Strain rate sensitivity and fracture mechanism of AlSi10Mg parts produced by Selective Laser Melting, Mater. Sci. Eng. A. 682 (2017) 509–517. https://doi.org/10.1016/j.msea.2016.11.070.

[37] S. Khan, R. Elliott, Quench modification of aluminium-silicon eutectic alloys, J. Mater. Sci. 31 (1996) 3731–3737. https://doi.org/10.1007/BF00352787.

[38] Y. Li, D. Gu, Parametric analysis of thermal behavior during selective laser melting additive manufacturing of aluminum alloy powder, Mater. Des. 63 (2014) 856–867. https://doi.org/10.1016/j.matdes.2014.07.006.

[39] H. Qin, Q. Dong, V. Fallah, M.R. Daymond, Rapid Solidification and Non-equilibrium Phase Constitution in Laser Powder Bed Fusion (LPBF) of AlSi10Mg Alloy: Analysis of Nano-precipitates, Eutectic Phases, and Hardness Evolution, Metall. Mater. Trans. A Phys. Metall. Mater. Sci. 51 (2020) 448–466. https://doi.org/10.1007/s11661-019-05505-5.

[40] D. Bouchard, J.S. Kirkaldy, Scaling of intragranular dendritic microstructure in ingot solidification, Metall. Mater. Trans. B Process Metall. Mater. Process. Sci. 27 (1996) 101–113. https://doi.org/10.1007/BF02915081.

[41] M. Tang, P.C. Pistorius, Anisotropic Mechanical Behavior of AlSi10Mg Parts Produced by Selective Laser Melting, Jom. 69 (2017) 516–522. https://doi.org/10.1007/s11837-016-2230-5.

[42] W. Li, S. Li, J. Liu, A. Zhang, Y. Zhou, Q. Wei, C. Yan, Y. Shi, Effect of heat treatment on AlSi10Mg alloy fabricated by selective laser melting: Microstructure evolution, mechanical properties and

Journal Pre-proof

fracture mechanism, Mater. Sci. Eng. A. 663 (2016) 116–125. https://doi.org/10.1016/j.msea.2016.03.088.

[43] E. Ghassemali, M. Riestra, T. Bogdanoff, B.S. Kumar, S. Seifeddine, Hall-Petch equation in a hypoeutectic Al-Si cast alloy: Grain size vs. secondary dendrite arm spacing, Procedia Eng. 207 (2017) 19–24. https://doi.org/10.1016/j.proeng.2017.10.731.

[44] A. Hadadzadeh, B.S. Amirkhiz, M. Mohammadi, Contribution of Mg2Si precipitates to the strength of direct metal laser sintered AlSi10Mg, Mater. Sci. Eng. A. 739 (2019) 295–300. https://doi.org/10.1016/j.msea.2018.10.055.

[45] Q. Zhao, B. Holmedal, The effect of silicon on the strengthening and work hardening of aluminum at room temperature, Mater. Sci. Eng. A. 563 (2013) 147–151. https://doi.org/10.1016/j.msea.2012.11.062.

[46] A. Hadadzadeh, B.S. Amirkhiz, A. Odeshi, M. Mohammadi, Dynamic loading of direct metal laser sintered AlSi10Mg alloy: Strengthening behavior in different building directions, Mater. Des. 159 (2018) 201–211. https://doi.org/10.1016/j.matdes.2018.08.045.

[47] S. Xia, Y. Qi, T. Perry, K.S. Kim, Strength characterization of Al/Si interfaces: A hybrid method of nanoindentation and finite element analysis, Acta Mater. 57 (2009) 695–707. https://doi.org/10.1016/j.actamat.2008.10.011.

[48] L. Zhao, J.G. Santos Macías, L. Ding, H. Idrissi, A. Simar, Damage mechanisms in selective laser melted AlSi10Mg under as built and different post-treatment conditions, Mater. Sci. Eng. A. 764 (2019) 1–25. https://doi.org/10.1016/j.msea.2019.138210.

Journal Pre-proof

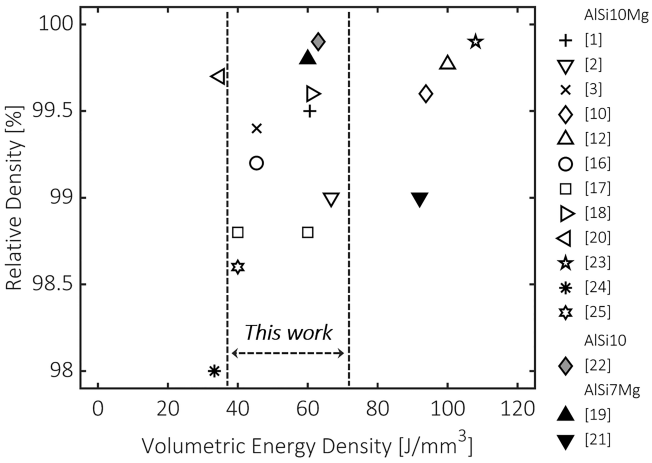

Journal Pre-proof

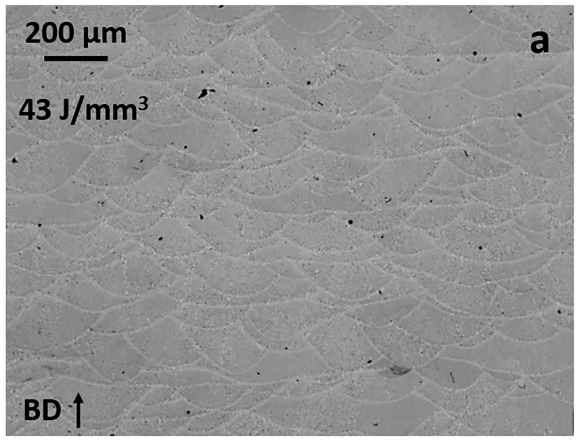
200 µm
a
43 J/mm³
BD

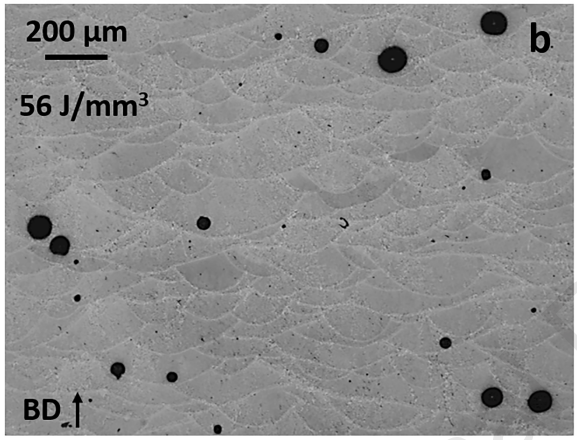
200 µm
b
56 J/mm³
BD

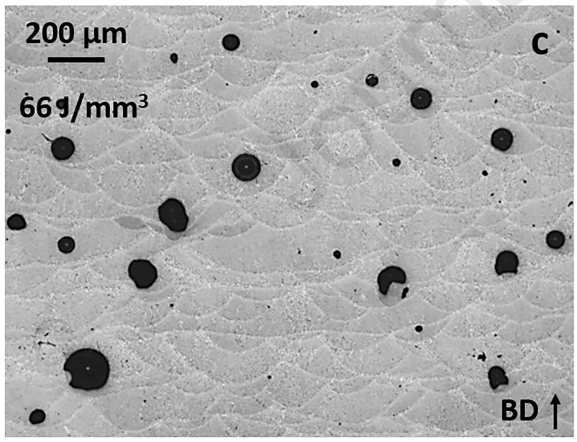
200 µm
c
66 J/mm³
BD

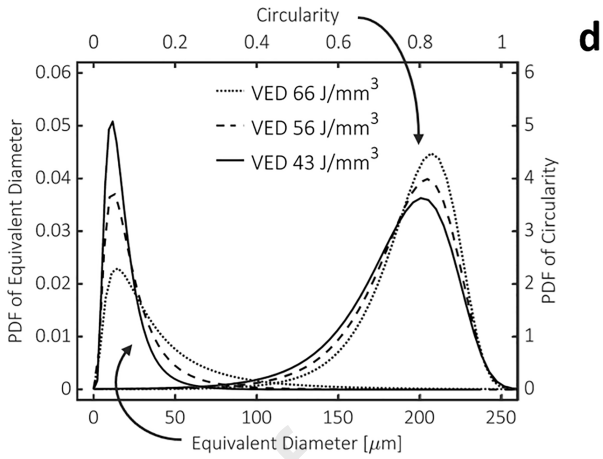
d
Circularity
0
0.2
0.4
0.6
0.8
1
VED 66 J/mm³
VED 56 J/mm³
VED 43 J/mm³
PDF of Equivalent Diameter
PDF of Circularity
Equivalent Diameter [µm]

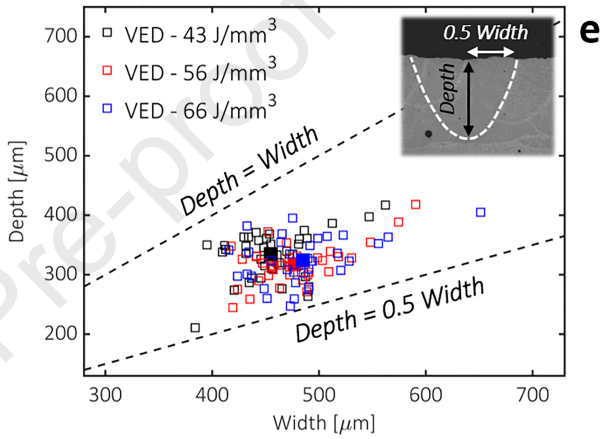
e
VED - 43 J/mm³
VED - 56 J/mm³
VED - 66 J/mm³
0.5 Width
Depth
Depth = Width
Depth = 0.5 Width
Depth [µm]
Width [µm]

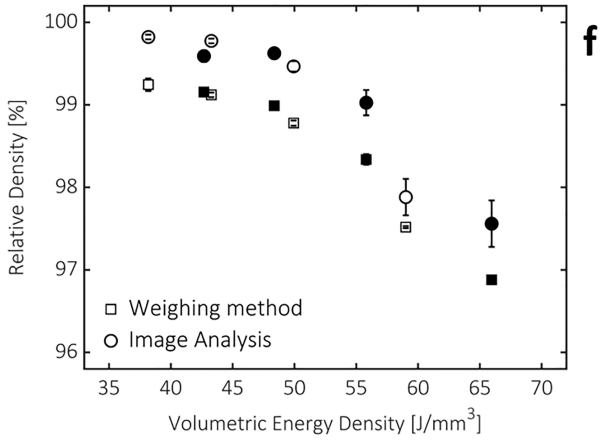
f
Relative Density [%]
Weighing method
Image Analysis
Volumetric Energy Density [J/mm³]

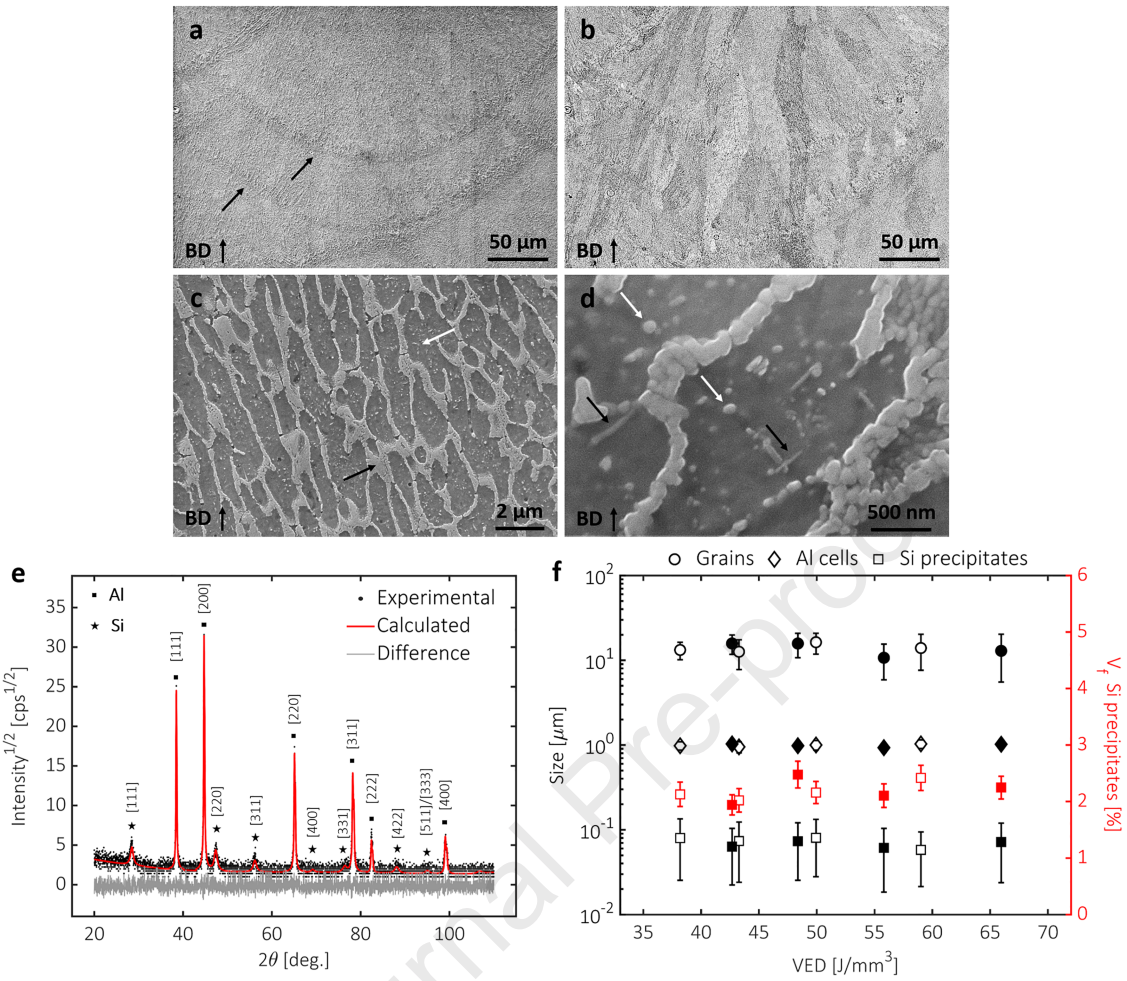

Journal Pre-proof

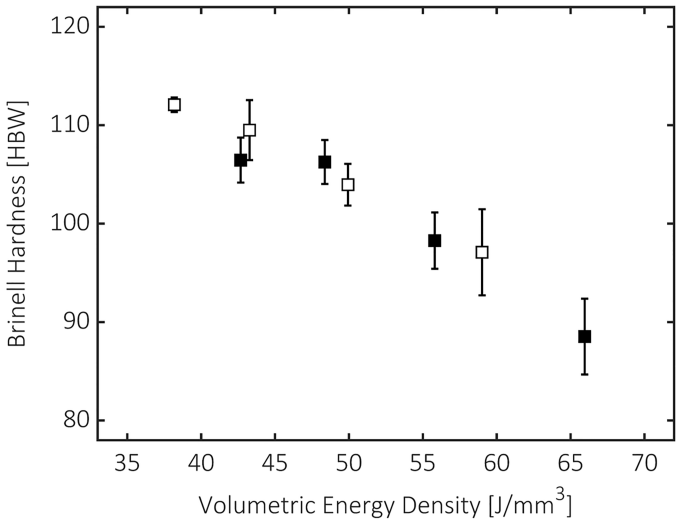

Journal Pre-proof

Journal Pre-proof

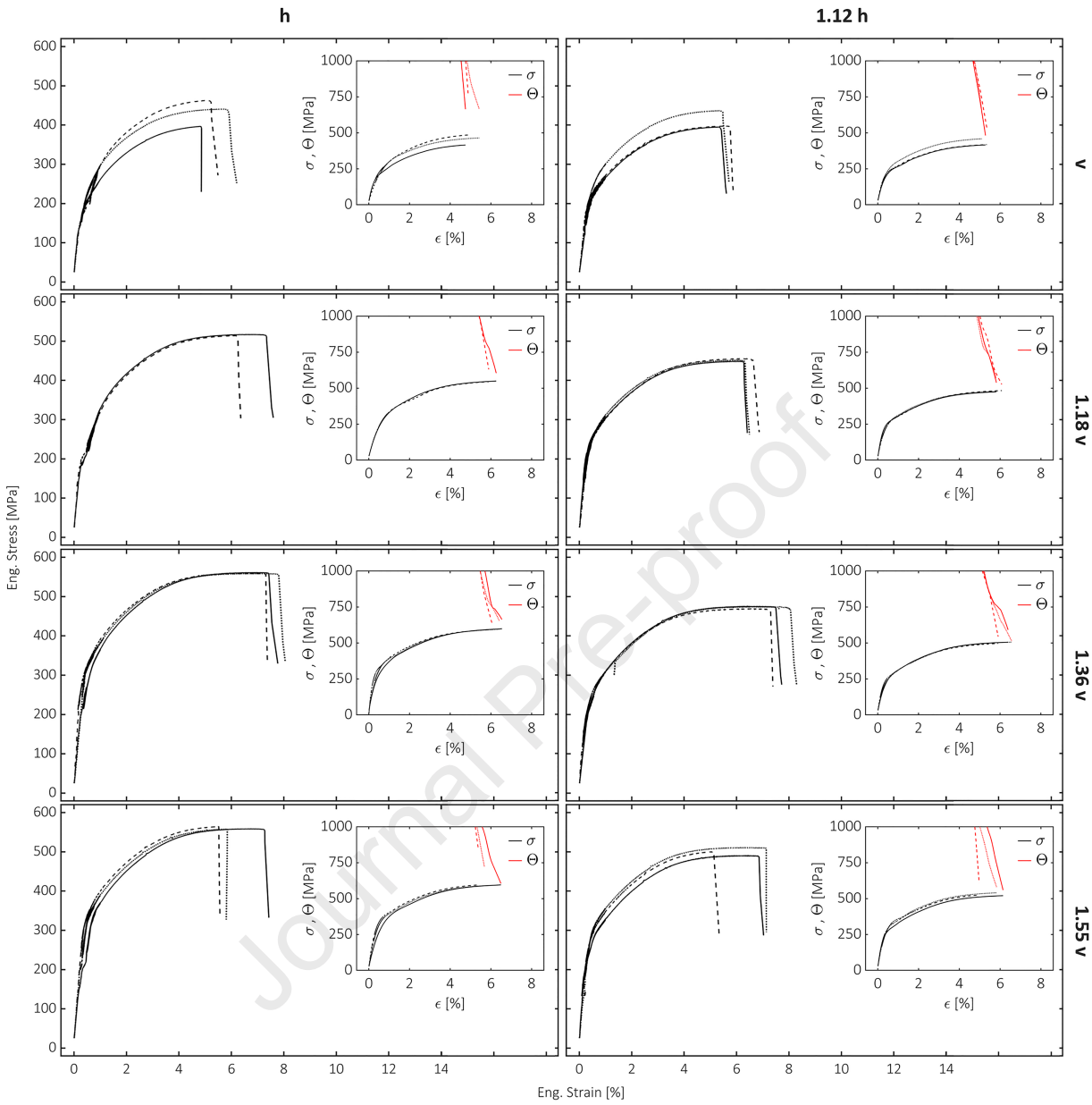

Journal Pre-proof

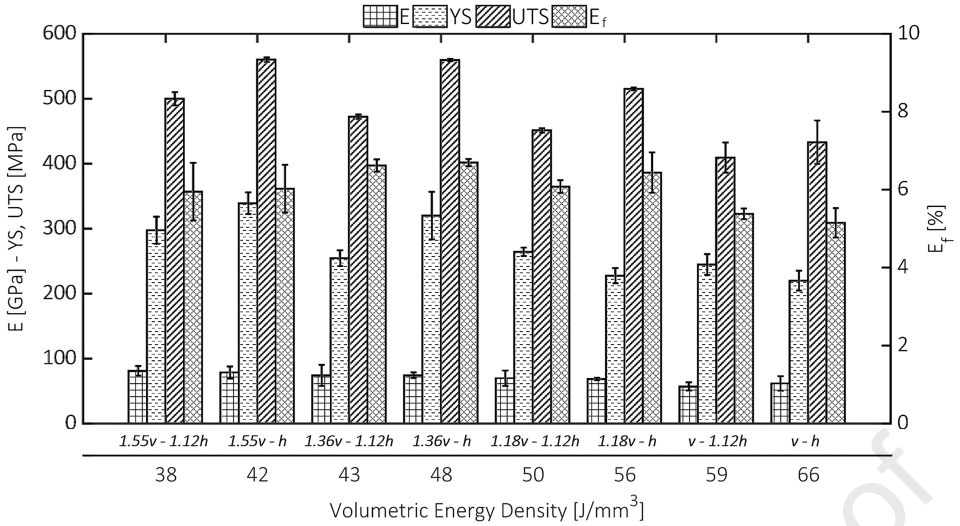

Journal Pre-proof

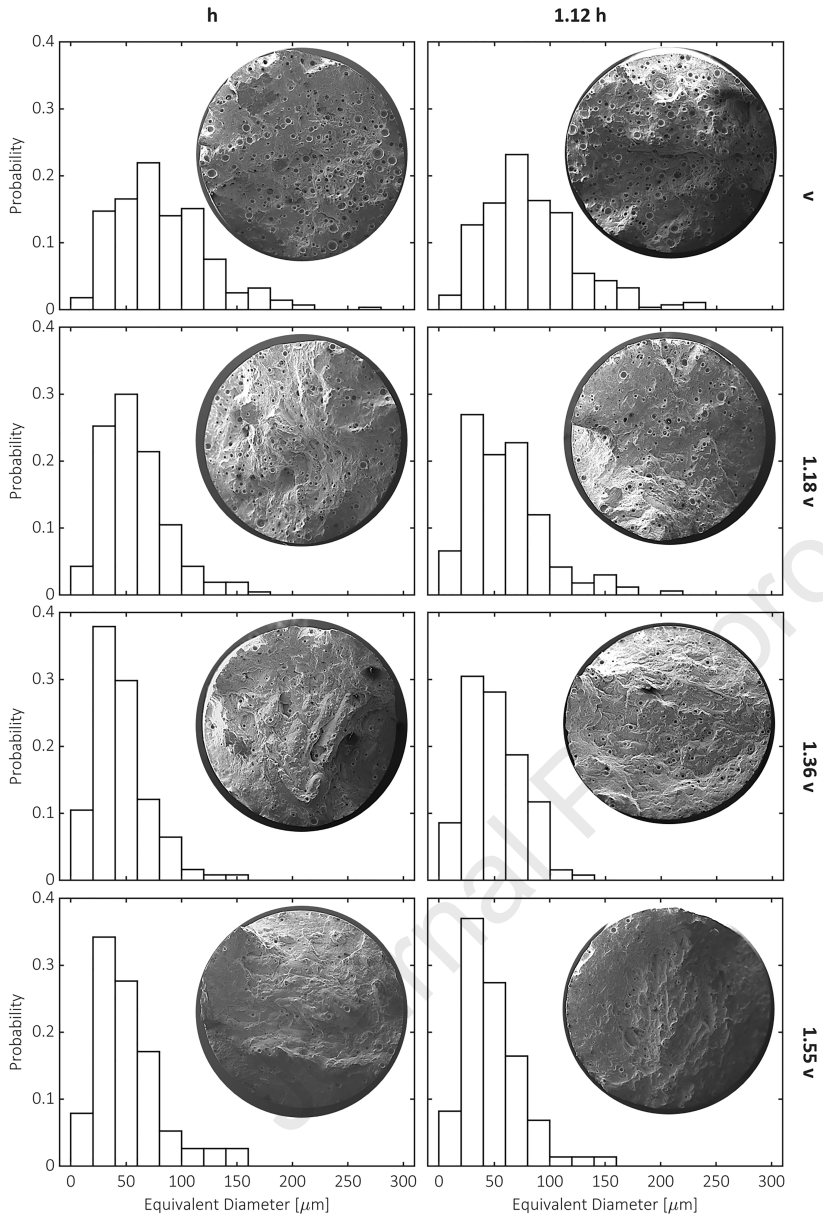

Journal Pre-proof

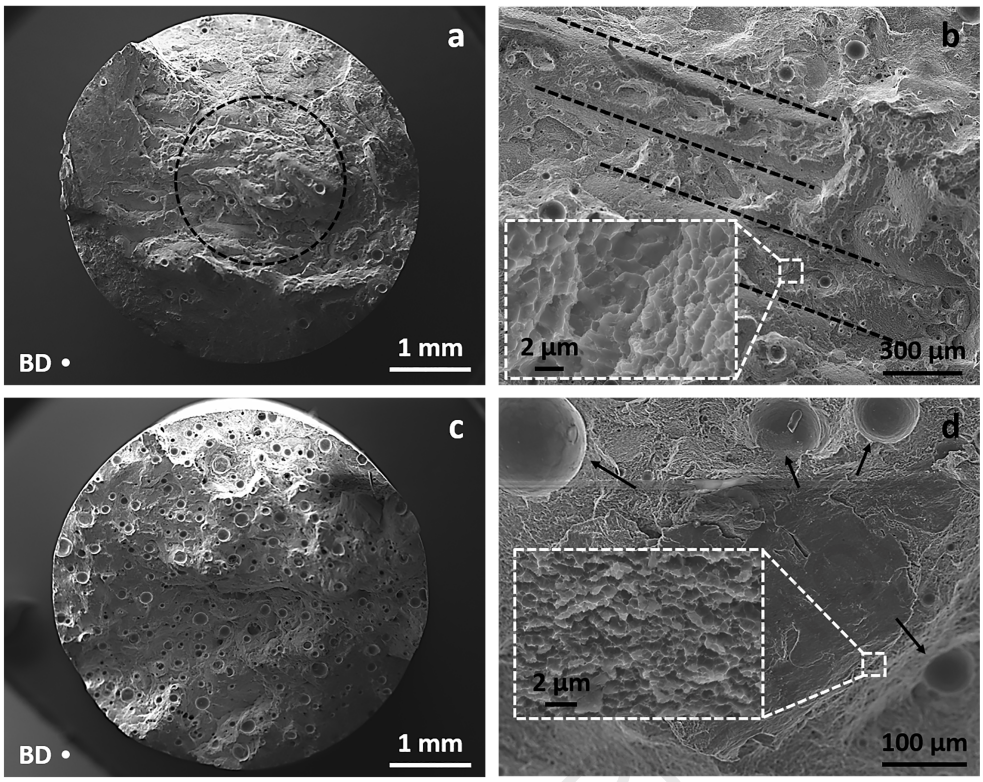

Journal Pre-proof

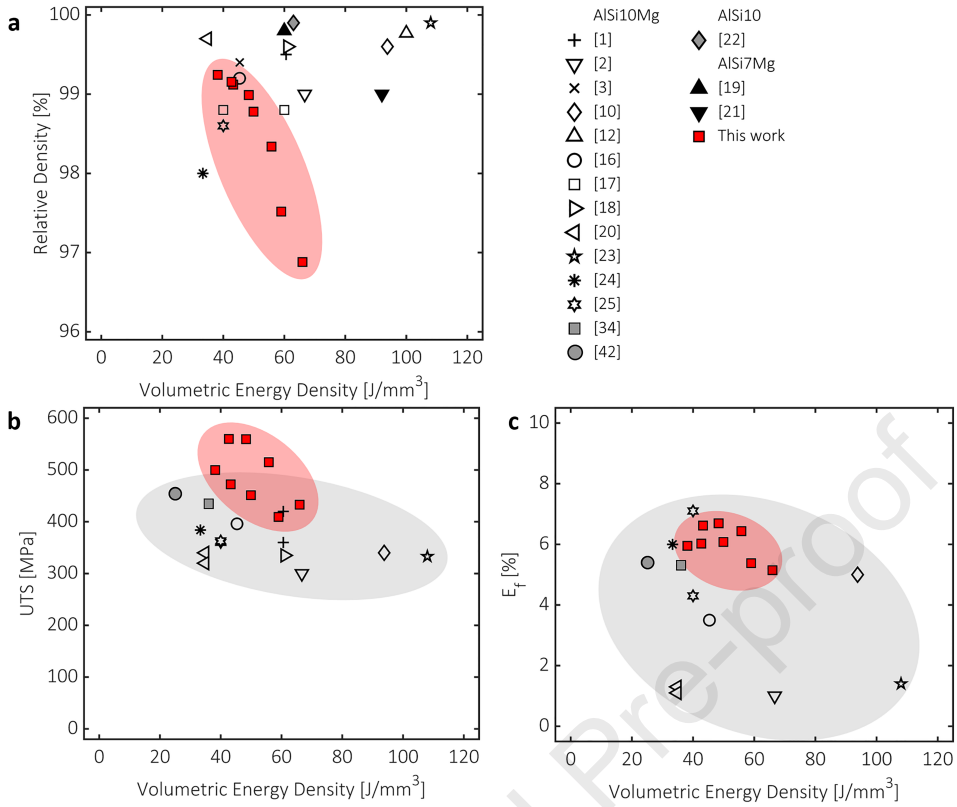

Journal Pre-proof

Author contributions

MG performed the SEM and XRD analyses, GS performed the hardness tests and density measurements, MG and GS did the samples' preparation, OM observations and image analysis calculations. MTDG acquired the additively manufactured specimens and performed the tensile tests. MM supervised the work and acquired funding. MG wrote the first draft of the manuscript. All the authors contributed to and read the final manuscript.

Journal Pre-proof

Journal Pre-proof

Declaration of interests

☒ The authors declare that they have no known competing financial interests or personal relationships that could have appeared to influence the work reported in this paper.

☐The authors declare the following financial interests/personal relationships which may be considered as potential competing interests:

Journal Pre-proof